WEP Warwick Evans Publishing

International Journal of Mechanical and Electrical Engineering

ISSN: 3005-9615 (Print), ISSN: 3005-7132 (Online)
Volume 8, Number 6, Year 2026
DOI: https://doi.org/10.62051/ijmee.v8n6.05

Sealing Failure Mechanism and Finite-Element Analysis of O-Ring Sealing-Behavior in a Core-Barrel Roller-Cone Bit Bearing

Yachao Ma *, Jinmao Yang, Jie Li, Bing Deng, Wei Zhang, Jianhui Yu

School of Mechatronic Engineering, Southwest Petroleum University, Chengdu, Sichuan, 610500, China

* Corresponding Author: Yachao Ma

ABSTRACT

Core-drilling roller-cone bit bearings operate under high pressure, solids-laden drilling fluid, and dynamic loading. HNBR O-rings isolate the lubricated bearing cavity from the external environment; their failure can cause rapid bearing wear and cone seizure. This study investigates the failure mechanism and sealing behavior of HNBR O-rings through uniaxial tensile testing, macroscopic observation, scanning electron microscopy (SEM), and nonlinear finite element analysis (FEA). The HNBR material exhibited an ultimate tensile strength of 17.24 MPa, an elastic modulus of 8.73 MPa, and an elongation at break of 342.24%. The third-order Yeoh model fitted the tensile response more accurately than the Mooney-Rivlin model and was adopted for FEA. Macroscopic and SEM observations revealed circumferential grooves and abrasion on the inner surface, abrasive wear, spalling, and particle adhesion on the outer surface, and laminar tearing with profile distortion on the lateral surface. A two-dimensional axisymmetric nonlinear contact model was used to evaluate the effects of compression ratio (11.5%-17.5%) and fluid pressure (1.0-1.5 MPa) on contact pressure, von Mises stress, and effective contact area. As the compression ratio increased from 11.5% to 17.5%, the maximum Contact Stress increased from 2.7712 MPa to 4.9585 MPa and the maximum von Mises stress increased from 1.2905 MPa to 2.0492 MPa. Contact Stress exceeded fluid pressure under all simulated conditions. Sealing surface 3, between the O-ring upper surface and the groove top face, exhibited the lowest Contact Stress and effective contact area and was identified as the weakest sealing region. A compression ratio of 14.5%-16% is recommended within the investigated range to balance sealing reliability and rubber stress. The results provide guidance for O-ring design, assembly control, and failure prevention in core-drilling roller-cone bit bearings.

KEYWORDS

Core-drilling Roller-cone Bit Bearing; HNBR O-ring; Sealing Failure; Hyperelastic Constitutive Model; Finite Element Analysis; Compression Ratio; Contact Pressure.

1. INTRODUCTION

Core barrel is widely used in mineral exploration, geological investigation, and foundation engineering because it provides relatively intact rock cores for geological evaluation and engineering decision-making. Roller-cone bits remain important tools in complex and abrasive formations because they can adapt to variable lithologies while transmitting substantial axial loads and torque. The bearing system inside the cone is a critical subsystem because it supports cone rotation under fluctuating mechanical loads, drilling-fluid pressure, and abrasive cuttings. Its reliability directly affects drilling efficiency, bit life, and operational safety. Once the bearing seal fails, drilling fluid

Content from this work may be used under the terms of CC BY-NC 4.0 licence (https://creativecommons.org/licenses/by-nc/4.0/).
Published by Warwick Evans Publishing.

and solid particles can enter the lubricated cavity, accelerate wear of the rolling elements and journal, degrade lubrication, and eventually cause bearing damage or cone seizure [1].

Elastomeric O-rings are commonly used to isolate the bearing cavity from the drilling environment and retain lubricating grease. Their performance depends on sufficient contact pressure, stable contact area, material integrity, and compatibility with the service medium. In roller-cone bit bearings, however, O-rings are not exposed to simple static sealing conditions. They undergo assembly compression, local contact stress, relative slip, geometric runout, pressure fluctuation, and particle-contaminated fluid. These coupled factors can redistribute Contact Stress and promote local stress concentration, abrasion, crack initiation, and permanent deformation. Therefore, the initial sealing state alone is insufficient for evaluating O-ring reliability.

Hydrogenated nitrile butadiene rubber (HNBR) is widely used in demanding oilfield sealing applications because it combines the oil resistance of nitrile rubber with improved thermal stability and mechanical strength. Hydrogenation reduces carbon-carbon double bonds in the butadiene segments and improves resistance to thermo-oxidative degradation. The mechanical properties and oil resistance of HNBR compounds depend on material formulation, including acrylonitrile content, carbon-black loading, and operating temperature [2]. However, HNBR may still deteriorate under long-term service. Elevated temperature can alter fatigue-crack-growth behavior and reduce the fatigue life of carbon-black-filled HNBR [3]. Accordingly, experimental characterization and appropriate constitutive modeling are required before evaluating HNBR seal performance numerically.

The fundamental requirement for O-ring sealing is that the interfacial Contact Stress remains higher than the applied fluid pressure along the effective sealing path. Because rubber sealing involves large deformation as well as material, geometric, and contact nonlinearities, finite element analysis is widely used to evaluate seal deformation, contact pressure, and stress distribution [4]. Numerical studies of hydraulic-buffer seals have shown that seal geometry and compression strongly affect contact behavior and structural performance [5]. Investigations of non-standard O-rings in subsea connectors have likewise demonstrated that seal geometry and contact conditions determine sealing reliability [6]. High-pressure sediment-sampler studies further show that local contact-pressure distribution is important because low-pressure zones may become leakage paths [7].

Surface condition and local geometric defects can further affect sealing behavior. Pits, scratches, and dimensional deviations may disrupt the continuity of the contact interface and increase leakage risk [8]. Studies of high-pressure and high-temperature packer elements have also shown that weak sealing regions must be identified and strengthened to maintain reliable Contact Stress under harsh downhole conditions [9]. These studies provide useful methodological references, but the geometry and loading conditions of roller-cone bit bearings differ from those of conventional hydraulic, subsea, and packer seals.

Research on roller-cone bit seals has primarily focused on bearing-seal optimization, novel seal structures, and metal face seals. Failure analysis of cone-bit bearing seals indicated that excessive compression can induce high shear stress and damage in rubber rings, while an unsuitable contact-pressure distribution can accelerate wear of mating metal seal rings [10]. A three-dimensional transient thermo-mechanical analysis of a novel rubber seal reported lower equivalent stress and improved stress distribution compared with a conventional O-ring configuration under high-temperature conditions [11]. Research on grid-shaped bionic non-smooth bearing-ring surfaces confirmed that rubber-ring wear remains an important factor in seal failure [12]. For flat rubber rings in roller bits, a modified Yeoh formulation improved the prediction of sealing behavior and equivalent stress [13]. These studies demonstrate the importance of constitutive modeling and contact analysis, but conventional HNBR O-rings in core-drilling roller-cone bit bearings remain insufficiently investigated.

The service environment of roller-cone bits is also dynamic. Periodic vibration and impact loading can influence instantaneous sealing performance by changing liquid-film distribution in metal seals [14]. Multi-field analyses of surface-textured metal seals have further highlighted the interaction among contact mechanics, temperature, lubrication, and surface structure [15]. Although these studies concern the same bearing environment, elastomeric O-rings differ from metal seals in their large local deformation and stress sensitivity. The coupled influence of assembly compression ratio and fluid pressure on individual O-ring sealing surfaces therefore requires separate evaluation.

Abrasive wear is particularly relevant when elastomeric seals contact solids-laden drilling fluid. In V-shaped sealing rings used in multistage fracturing tools, compression set and abrasive wear were identified as major degradation modes [16]. In rubber/steel sealing pairs, particle breakage during abrasive wear can change contact morphology and wear mechanisms [17]. Wear characteristics may also change with particle size and Contact Stress [18]. For O-ring seals under three-body abrasion, non-uniform particle size affects friction and surface damage [19]. These findings are relevant to roller-cone bit O-rings because cuttings and debris may enter the sealing interface and promote abrasion, spalling, and crack development.

Reliable finite element analysis also requires a constitutive model suitable for the tested rubber compound. Hyperelastic models, including Mooney-Rivlin, Yeoh, Neo-Hookean, and Ogden models, describe large rubber deformation through strain-energy density functions. The Ogden model has been influential in nonlinear elasticity because it represents rubber behavior using principal stretches [20]. Revised Yeoh-type models have also been developed for nearly incompressible rubber materials to improve volumetric treatment and fitting accuracy [21]. Nevertheless, the appropriate model depends on material formulation, test data, and deformation range. A direct comparison of candidate models is therefore necessary for the HNBR O-ring examined in this study.

Despite previous work, several issues remain unresolved. First, the failure morphology of HNBR O-rings in core-drilling roller-cone bit bearings has rarely been evaluated systematically across the inner, outer, and lateral surfaces using both macroscopic observation and SEM. Second, the effects of compression ratio and fluid pressure on contact pressure, von Mises stress, and effective contact area at multiple sealing surfaces have not been sufficiently quantified for the bearing-groove geometry considered here. Third, the weakest sealing interface and an appropriate compression-ratio range balancing sealing performance and excessive rubber stress remain unclear. Recent thermo-mechanical studies of O-rings also indicate the importance of coupled loading in seal-reliability assessment [22].

Accordingly, this study combines uniaxial tensile testing, failure-morphology characterization, and nonlinear finite element analysis to investigate HNBR O-rings used in core-drilling roller-cone bit bearings. The objectives are to: (i) determine the hyperelastic response of the HNBR material and select a constitutive model by comparing the Mooney-Rivlin and third-order Yeoh models; (ii) identify region-specific failure features through macroscopic observation and SEM; (iii) evaluate the effects of compression ratio and fluid pressure on contact pressure, von Mises stress, and effective contact area at three sealing surfaces; and (iv) identify the weakest sealing surface and recommend a compression-ratio range under the investigated conditions. The results provide experimentally informed guidance for seal design, assembly control, and failure prevention.

2. MATERIAL CHARACTERIZATION AND FAILURE ANALYSIS

2.1. Determination of HNBR Material Parameters

2.1.1. Uniaxial Tensile Test

Uniaxial tensile tests were conducted using a universal testing machine. Strip specimens were cut from an unused, intact O-ring and clamped in the test fixtures. The machine stretched the specimens

at a constant rate of 500 mm/min, ensuring consistent loading direction and boundary conditions throughout the test. Stress and strain data were acquired synchronously to construct the material stress–strain curve, thereby characterizing the overall deformation behavior of the O-ring material.

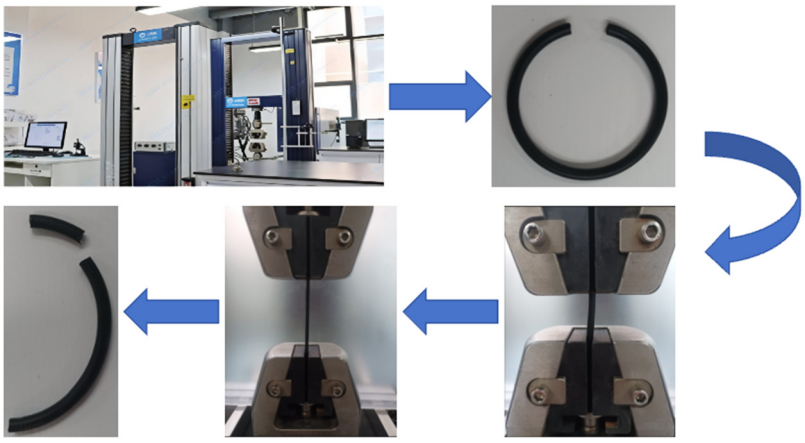


Figure 1. Experimental procedure

The tensile test results are summarized in Table 1. The O-ring material sustained large deformation during stretching, with a maximum elongation at break of 342.24%. Its stress–strain curve (Fig. 2) exhibited pronounced nonlinearity. Consequently, a nonlinear elastic model is required to accurately describe the mechanical and deformation behavior of the O-ring under actual sealing conditions.

Table 1. Mechanical properties of the HNBR O-ring material from the tensile test.

Property	Value
Ultimate tensile strength (MPa)	17.24
Elastic modulus (MPa)	8.73
Elongation at break ($\%$)	342.24
Hardness (Shore A)	75

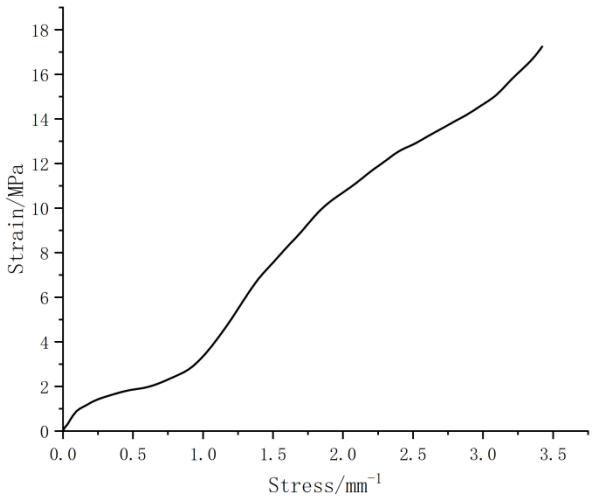


Figure 2. Engineering stress-strain curve of the HNBR O-ring material.

2.1.2. Hyperelastic Constitutive Model Fitting

The hyperelastic behavior of rubber is characterized by a strain energy density function W, which relates the strain energy to the deformation invariants. In this study, two commonly used constitutive models—the Mooney–Rivlin model and the Yeoh model—were fitted to the experimental stress–strain data.

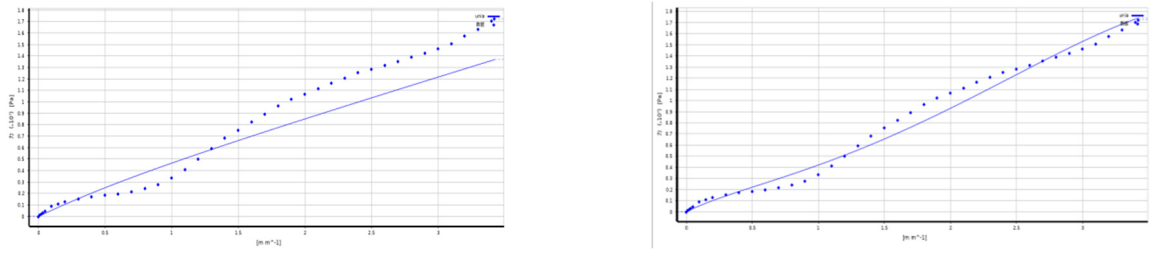
The strain energy density function of the two-parameter Mooney–Rivlin model is expressed as:

$$W = C_{10}(I_1 - 3) + C_{01}(I_2 - 3)$$

The strain energy density function of the Yeoh model is expressed as:

$$W = C_{10}(I_1 - 3) + C_{20}(I_1 - 3)^2 + C_{30}(I_1 - 3)^3$$

The fitting curves in Fig. 3 demonstrate that the third-order Yeoh model provides a better fit to the experimental data than the Mooney–Rivlin model, particularly in the moderate-to-large deformation regime. Accordingly, the third-order Yeoh model was selected as the constitutive model for subsequent finite element analysis. The determined material parameters are listed in Table 2.



3a. Fitting curve of the Mooney-Rivlin model 3b. Fitting curve of the Yeoh model

Figure 3. Comparison between Mooney–Rivlin model and third-order Yeoh model in fitting experimental data

Table 2. Third-order Yeoh model parameters for HNBR

C_{10} (MPa)	C_{20} (MPa)	C_{30} (MPa)	D_1 (MPa^{-1})	D_2 (MPa^{-1})	D_3 (MPa^{-1})
0.97985	0.058477	−0.001126	0.0011	0	0

2.2. Failure Analysis of the O-Ring Seal

2.2.1. Macroscopic Morphology Analysis



4a. Inner Circle 4b. Outer Circle 4c. Side view

Figure 4. Macroscopic failure morphologies on each surface of the failed O-ring

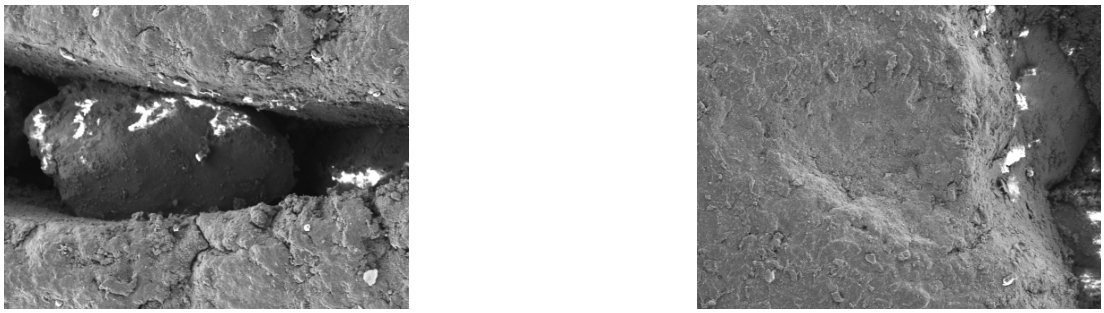
Macroscopic observation of the failed O-ring (Fig. 4) revealed region-specific surface damage with varying severity. The inner surface exhibited circumferential grooves accompanied by abrasion marks

and impurity adhesion, indicating groove wear caused by repeated slip at the mating interface. The outer surface was rough and displayed localized spalling, impurity deposition, and edge tearing defects, suggesting significant frictional shear and erosive wear by drilling cuttings. The lateral surface sustained the most severe damage, with evident tearing, flaky spalling, and profile distortion, attributable to the combined action of seal groove extrusion, bearing axial runout, and lateral shear friction. Overall, the outer and lateral surfaces were the most heavily damaged regions, whereas the inner surface experienced relatively mild wear. The failure is attributed to the coupled effects of assembly compression, contact pressure, interfacial slip, and abrasive wear.

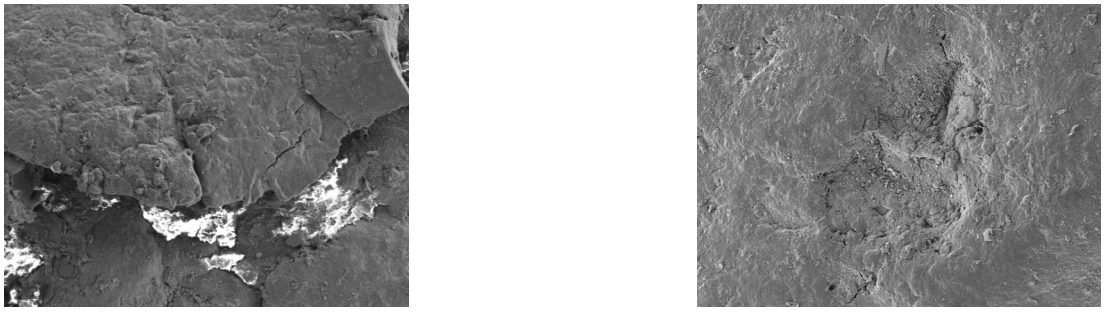
2.2.2. SEM Microscopic Morphology Analysis

Scanning electron microscopy (SEM) was employed to examine the microscopic damage features of the failed O-ring at magnifications of 100× and 1000×.

At 100× magnification, the overall damage distribution was clearly resolvable. The inner surface was rough and uneven, with spalling, cracks, pits, and particle adhesion. The outer surface exhibited an undulating topography with spalling and particle accumulation, with damage propagating from the surface layer outward. The lateral surface showed the initiation of linear cracks and laminar delamination, primarily induced by shear and interfacial debonding. The distinct regional characteristics indicate that the inner and outer surfaces are dominated by surface spalling and material loss, whereas the lateral surface is characterized by cracking and interlayer delamination.



5a. SEM morphology of the inner-ring surface at 100× magnification



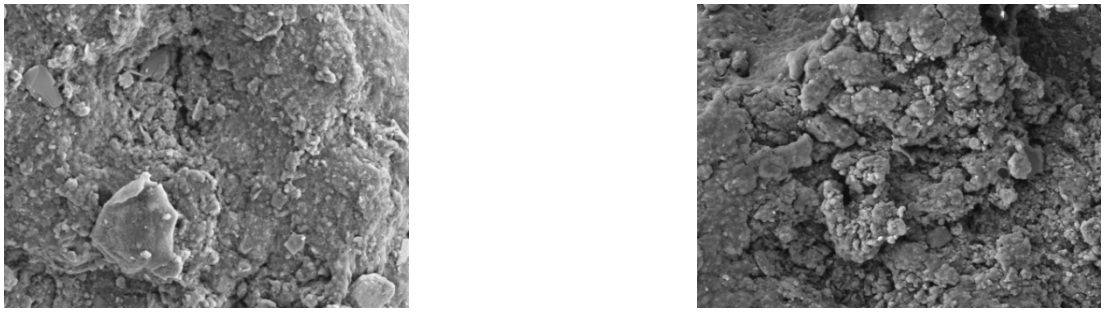
5b. SEM morphology of the outer-diameter surface at 100× magnification



5c. SEM morphology of the lateral surface at 100× magnification

Figure 5. SEM morphologies of each surface of the failed O-ring at a magnification of 100×

At 1000× magnification, the O-ring surface layer appeared loose and fragmented, with extensive flaky spalling, debris accumulation, and irregular cracks, indicating severe surface delamination. The outer surface was rough and distributed with adherents, cracks, and pits, resulting from the synergistic action of frictional shear and hard particles. The lateral surface exhibited laminar tearing, flaky detachment, and debris accumulation, caused by localized shear and interfacial debonding. The microanalysis confirms that the overall damage is induced by the combined action of frictional wear and localized shear.



6a.SEM morphology of the inner-ring surface at 1000× magnification



6b.SEM morphology of the outer-diameter surface at 1000× magnification



6c.SEM morphology of the lateral surface at 1000× magnification

Figure 6. SEM morphologies of each surface of the failed O-ring at a magnification of 1000×

The SEM observations confirm severe surface degradation of the failed O-ring. The inner and outer surfaces exhibited material loss, spalling, surface cracks, pits, and particle adhesion, whereas the lateral surface showed laminar tearing, flaky detachment, and debris accumulation. These features indicate that frictional wear and localized shear played important roles in the observed surface damage.

3. FINITE ELEMENT ANALYSIS OF O-RING SEALING BEHAVIOR

3.1. Geometric Model and Material Parameters

A simplified two-dimensional axisymmetric model was adopted, with the specific dimensions shown in Fig. 7. The cone body and shaft were made of 15MnNi4Mo steel, and the O-ring was made of

hydrogenated nitrile butadiene rubber (HNBR). The material parameters of the O-ring are listed in Table 2, and those of the metallic cone body and shaft are listed in Table 3.

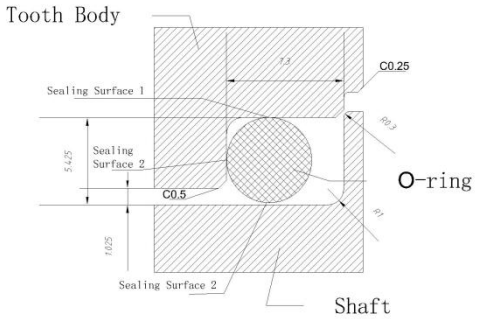


Figure 7. Dimensions of the Simulation Model Structure

Table 3. Material parameters of the sealing components.

Component	Material	Density (kg/m³)	Elastic modulus (MPa)	Poisson's ratio
Cone body, shaft	15MnNi4Mo	7850	2.05×10^5	0.3

3.2. Basic Assumptions

To facilitate the finite element analysis while preserving the essential physical characteristics of the sealing problem, the following simplifying assumptions were adopted:

1) The rubber material is treated as isotropic, homogeneous, and fully hyperelastic, with its mechanical behavior fully described by the third-order Yeoh constitutive model.

2) Stress relaxation and creep of the rubber material are neglected, as the analysis focuses on the quasi-static mechanical response under assembly compression and fluid pressure loading.

3) The effects of formation temperature and bearing frictional heating on the sealing performance of the O-ring are not considered.

4) The stiffness of the cone body and journal is much greater than that of the O-ring; therefore, deformation of the metallic components is neglected and they are treated as rigid bodies.

The neglect of temperature effects and viscoelastic behavior represents a simplification that will be addressed in future work.

3.3. Contact Settings and Mesh Independence Verification

Following the rules for rigid–flexible contact pair definition and the subsequent fluid pressure boundary condition setup, four frictional contact pairs were defined with a friction coefficient of 0.2. A friction coefficient of 0.2 is a representative value for lubricated rubber–steel contact and is widely adopted in O-ring seal simulations. The four contact pairs are: (1) O-ring left lateral surface–cone groove left lateral surface (sealing surface 1); (2) O-ring right lateral surface–cone body side surface (sealing surface 2); (3) O-ring upper surface–cone body groove top surface (sealing surface 3); and (4) O-ring lower surface–shaft surface. All contact pairs were set as frictional contacts using the penalty algorithm.

Tetrahedral meshes were employed throughout the model. Five key metrics were selected for convergence assessment: equivalent elastic strain, equivalent (von Mises) stress, and the maximum Contact Stress on the three sealing surfaces. All relative errors during mesh refinement were below 5%, indicating that the selected mesh size achieved mesh independence. Balancing accuracy and computational efficiency, the final mesh sizes were: 0.4 mm for the cone body and journal, 0.15 mm

for the refined contact edges of the rigid bodies, and 0.1 mm for the seal ring. The meshed model is shown in Fig. 8.

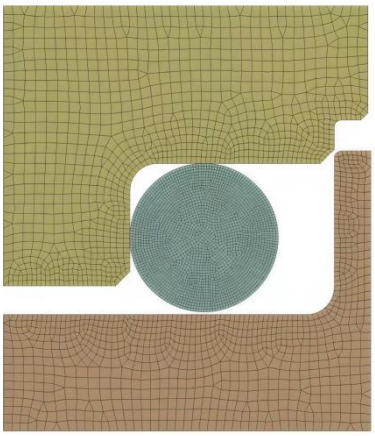
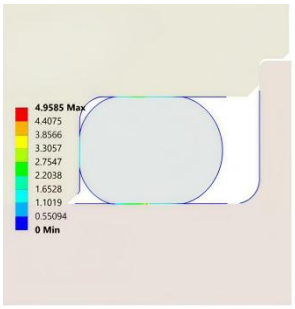


Figure 8. Mesh generation

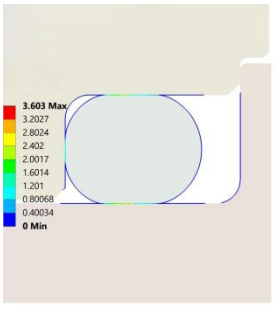
3.4. Effect of Assembly Compression Ratio on Sealing Performance

3.4.1. Effect of Compression Ratio on Maximum Contact Stress of Sealing Surfaces

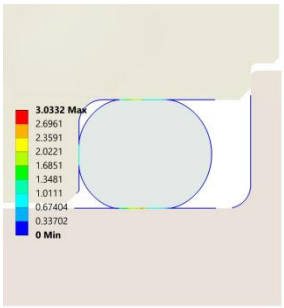
A fixed constraint was applied to the bearing base, and a downward displacement was imposed on the cone body to compress the O-ring to the target compression ratio. Five compression ratios were investigated: 17.5%, 16%, 14.5%, 13%, and 11.5%, corresponding to displacement values of 1.025, 0.95, 0.8685, 0.789, and 0.7095 mm, respectively. The nominal compression ratio is 16%; due to radial runout of the cone body and manufacturing tolerances, the actual maximum and minimum compression ratios are approximately 17.5% and 11.5%, respectively.

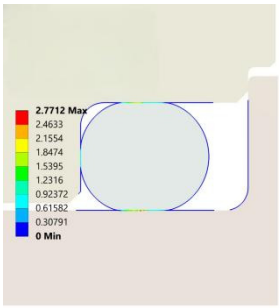






9a. Compression ratio of 17.5 % 9b. Compression ratio of 16 % 9c. Compression ratio of 14.5 %





9d. Compression ratio of 13% 9e. Compression ratio of 11.5%

Figure 9. Contour plots of Contact Stress distribution at different compression ratios

The contact stress distribution contours at different compression ratios are shown in Fig. 9. Under all five compression ratios, the contact stress of the O-ring exhibited a non-uniform distribution characterized by "high at the edges and low at the center," with high-stress regions concentrated at the interfaces between the O-ring and the metal groove walls and relatively low stress in the inner core region. As the compression ratio decreased from 17.5% to 11.5%, the high-stress regions at the upper and lower contact interfaces gradually contracted from large continuous areas to discontinuous patches and eventually to localized small regions, and the maximum contour contact stress decreased from 4.9585 MPa to 2.7712 MPa, indicating that increasing the compression ratio enhances the extrusion between the O-ring and the sealing components. Notably, the high-stress region at the upper contact surface (sealing surface 3) was smaller than that at the lower contact surface under all compression ratios and shrank more markedly with decreasing compression ratio, directly reflecting that sealing surface 3 is the weakest sealing location from the contour distribution perspective.

As shown in Fig. 10, the maximum contact stress on sealing surfaces 1, 2, and 3 all increased with increasing compression ratio, and throughout the entire compression ratio range the order was consistently sealing surface 2 > sealing surface 1 > sealing surface 3. The maximum contact pressure, corresponding to sealing surface 2, increased from 2.7712 MPa at a compression ratio of 11.5% to 4.9585 MPa at 17.5%. Sealing surface 3 consistently exhibited the lowest contact pressure, indicating relatively weak contact conformity and identifying this location as a potential weak region in the sealing structure. Therefore, moderately increasing the compression ratio is beneficial for enhancing the contact action at the sealing interface, but an excessively high compression ratio also increases the internal stress level of the rubber.

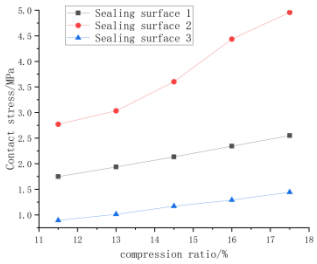
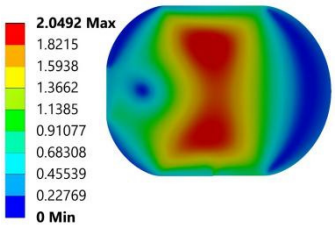
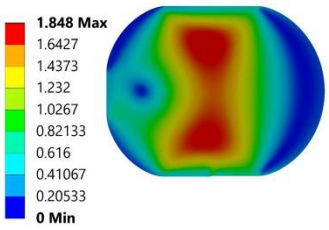
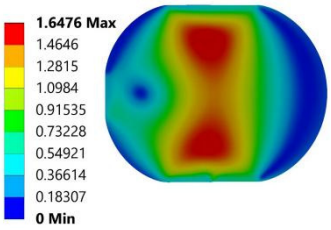


Figure 10. Variation of contact stress on each sealing surface with compression ratio

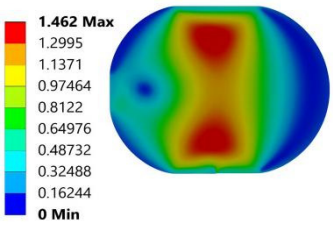
3.4.2. Effect of Compression Ratio on von Mises Stress of the O-Ring

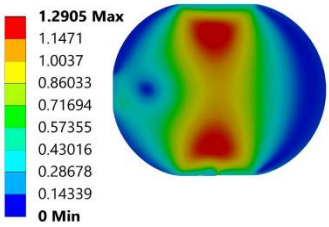






11a. Compression ratio of 17.5 % 11b. Compression ratio of 16 % 11c. Compression ratio of 14.5 %





11d. Compression ratio of 13% 11e. Compression ratio of 11.5%

Figure 11. Contour plots of von Mises stress distribution at different compression ratios

The von Mises stress contours of the O-ring at different compression ratios are shown in Fig. 11. Unlike contact stress, the high von Mises stress regions appeared not only at the contact interfaces but also extended to a certain depth into the O-ring interior, forming a "high-stress shell layer" distributed along the contact interfaces, with the lowest stress in the central region, indicating that the deformation energy induced by assembly compression is concentrated primarily in the surface-layer material. As the compression ratio decreased from 17.5% to 11.5%, the high-stress region gradually converged from a relatively extensive distribution to localized areas near the upper and lower contact interfaces, and the maximum von Mises stress decreased from approximately 2.0492 MPa to approximately 1.2905 MPa.

As shown in Fig. 12, the overall von Mises stress of the O-ring increased approximately linearly with the assembly compression ratio; when the compression ratio increased from 11.5% to 17.5%, the maximum von Mises stress increased from approximately 1.2905 MPa to 2.0492 MPa. The stress was consistently concentrated in the contact regions with the upper and lower groove walls, which were identified as high-risk failure zones. Although increasing the compression ratio enhances the sealing compression effect, it also elevates the rubber stress level, increasing the risk of tearing and permanent deformation in the high-stress regions. Therefore, the compression ratio must be selected reasonably to ensure that the Contact Stress meets anti-leakage requirements while avoiding excessive stress that accelerates aging and damage.

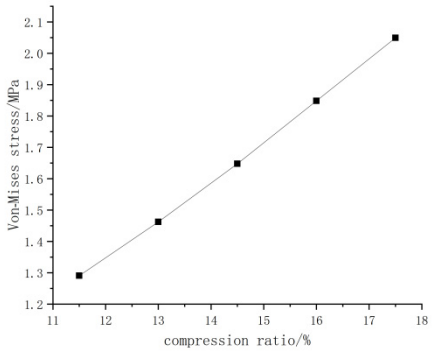


Figure 12. Variation of von Mises stress of the O-ring with compression ratio

3.4.3. Effect of Compression Ratio on Effective Contact Area of Sealing Surfaces

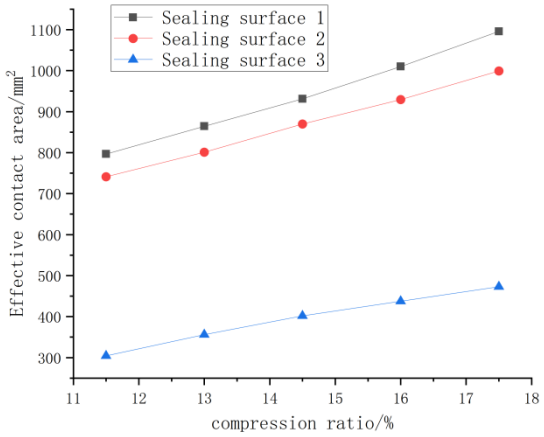


Figure 13. Variation of contact area on different contact surfaces with compression ratio

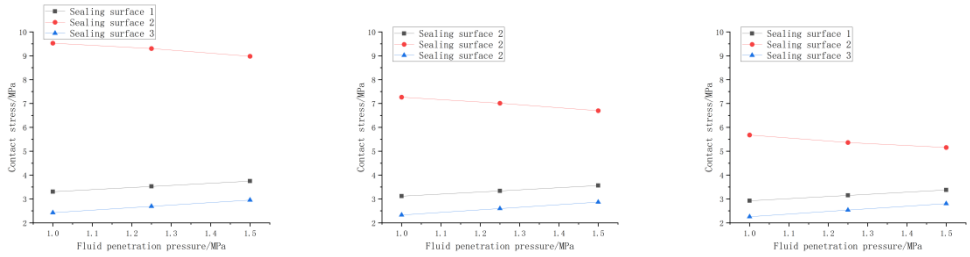
The effective contact areas of all three sealing surfaces increased with increasing compression ratio, as shown in Fig. 13. For sealing surfaces 1 and 2, the area increased continuously from 11.5% to 17.5%. For sealing surface 3, the area tended to plateau after the compression ratio reached 16%. In cross-comparison, sealing surface 1 had the largest contact area, followed by sealing surface 2, while

sealing surface 3 had the smallest overall. Sealing surface 3 is most prone to leakage due to insufficient conformity. When the compression ratio exceeds 16%, the increase in contact area slows, whereas the rubber stress continues to rise, exacerbating the risks of permanent deformation, wear, and cracking.

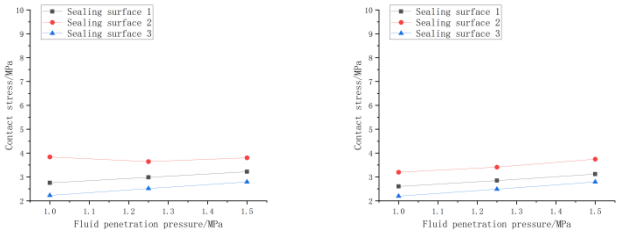
3.5. Sealing Performance under Coupled Fluid Penetration Pressure and Assembly Compression Ratio

3.5.1. Effect of Fluid Penetration Pressure on Maximum Contact Stress at Different Compression Ratios

Within the compression ratio range of 11.5%–17.5% and fluid pressure range of 1.0–1.5 MPa, the maximum Contact Stress on the three sealing surfaces followed the order: sealing surface 2 > sealing surface 1 > sealing surface 3, as shown in Fig. 14. Under all operating conditions, the Contact Stress exceeded the fluid pressure, confirming effective sealing. The Contact Stress on sealing surfaces 1 and 3 increased monotonically with fluid pressure. At compression ratios ≥ 13%, the Contact Stress on sealing surface 2 decreased slowly with increasing fluid pressure; at a compression ratio of 11.5%, it increased with increasing fluid pressure The compression ratio determines the Contact Stress baseline: high compression yields a higher initial preload but tends to induce excessive rubber stress, whereas low compression relies on the fluid self-energizing effect to reinforce sealing performance.



14a. Compression ratio of 17.5 % 14b. Compression ratio of 16 % 14c. Compression ratio of 14.5 %



14d. Compression ratio of 13% 14e. Compression ratio of 11.5%

Figure 14. Effect of fluid penetration pressure on the maximum Contact Stress of the sealing surfaces

3.5.2. Effect of Fluid Penetration Pressure on von Mises Stress at Different Compression Ratios

The von Mises stress of the O-ring increased approximately linearly with increasing compression ratio, as shown in Fig. 15. At the same compression ratio, higher fluid pressure yielded greater equivalent stress. In the low-compression regime, fluid pressure had a significant effect on stress; in the high-compression regime, assembly compression played the dominant role. The compression ratio and fluid pressure jointly elevate the internal stress of the rubber, and the risk of fatigue failure is highest under high-pressure, high-compression conditions.

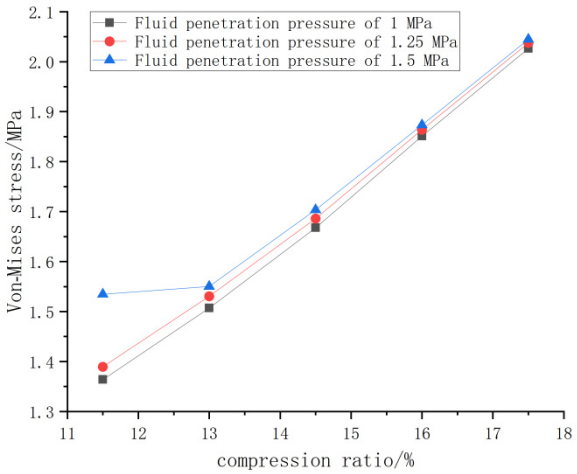
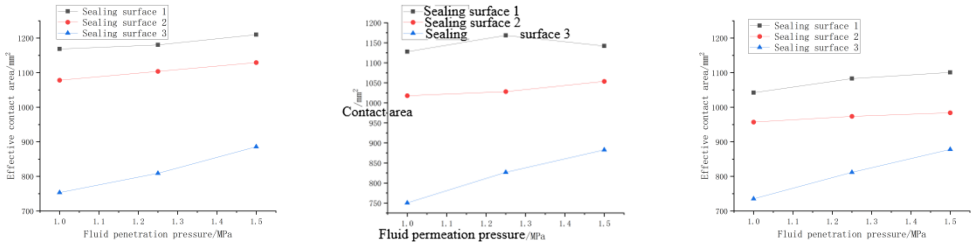


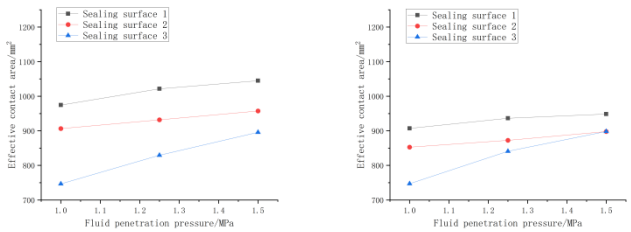
Figure 15. Variation of von Mises stress with fluid penetration pressure and compression ratio

3.5.3. Effect of Fluid Penetration Pressure on Effective Contact Area at Different Compression Ratios

Within the compression ratio range of 11.5%–17.5%, increasing fluid pressure generally enhanced the contact area on all three sealing surfaces, with the increase on sealing surface 3 far exceeding that on sealing surfaces 1 and 2, as shown in Fig. 16. The compression ratio determines the contact area baseline: higher compression yields a larger initial conformity area; lower compression makes sealing surface 3 more sensitive to fluid pressure. Only at a compression ratio of 16% did high fluid pressure cause the contact area of sealing surface 1 to first increase and then decrease; under all other compression ratios, the contact area of every sealing surface increased monotonically with fluid pressure.



16a. Compression ratio of 17.5 % 16b. Compression ratio of 16 % 16c. Compression ratio of 14.5 %



16d. Compression ratio of 13% 16e. Compression ratio of 11.5%

Figure 16. Effect of fluid penetration pressure on the contact area of the sealing surface

Overall, a compression ratio of 14.5%–16% is compatible with the full fluid pressure range of 1.0–1.5 MPa, balancing sufficient contact area and pressure adaptability while avoiding stress overload

at high compression and leakage risk at low compression. Sealing surface 3 is the primary weak location, and under low-pressure conditions sufficient compression is required to ensure conformity.

4. CONCLUSION AND OUTLOOK

This study investigated the failure mechanism and sealing behavior of HNBR O-rings in core-drilling roller-cone bit bearings through tensile testing, macroscopic observation, SEM, and nonlinear FEA. The main conclusions are as follows.

(1) The HNBR O-ring exhibited nonlinear hyperelastic behavior, with an ultimate tensile strength of 17.24 MPa, an elastic modulus of 8.73 MPa, and an elongation at break of 342.24%. The third-order Yeoh model described the measured response more accurately than the Mooney-Rivlin model and was selected for FEA.

(2) The failed O-ring exhibited region-specific damage. The inner surface showed circumferential grooves and abrasion; the outer surface exhibited abrasive wear, spalling, and particle adhesion; and the lateral surface showed the most severe damage, including laminar tearing and profile distortion. These features are consistent with the combined effects of assembly compression, contact pressure, interfacial slip, abrasive particles, axial runout, and lateral shear.

(3) As the compression ratio increased from 11.5% to 17.5%, the maximum Contact Stress increased from 2.7712 MPa to 4.9585 MPa, and the maximum von Mises stress increased from 1.2905 MPa to 2.0492 MPa. The effective contact area of each sealing surface increased with compression ratio. Above 16%, contact-area growth slowed while rubber stress continued to increase.

(4) Under fluid pressures of 1.0-1.5 MPa, the Contact Stress exceeded fluid pressure in all simulations. Fluid pressure generally increased the effective contact area and von Mises stress. Sealing surface 3, between the O-ring upper surface and the groove top face, consistently had the lowest Contact Stress and effective contact area and was identified as the weakest sealing region.

(5) Within the investigated conditions, a compression ratio of 14.5%-16% is recommended because it provides sufficient Contact Stress and contact area while avoiding the higher stress associated with excessive compression.

The present model is two-dimensional, axisymmetric, quasi-static, and isothermal. It does not consider viscoelasticity, stress relaxation, creep, wear evolution, surface roughness, temperature-dependent material properties, frictional heating, dynamic loading, axial runout, or three-dimensional effects. Future work should develop three-dimensional transient models incorporating rotation, vibration, runout, and time-varying pressure. Temperature-dependent viscoelastic behavior and particle-induced wear should be included, and the recommended compression ratio and weak sealing surface should be verified through bench and field tests.

ACKNOWLEDGMENTS

This work was financially supported by the National Natural Science Foundation of China (Nos. 2024JJ6181 and 51904263).

REFERENCES

[1] Huang, Z. Q., et al. (2018). Optimization of cone bit bearing seal based on failure analysis. Advances in Mechanical Engineering, 10(3), 320–331. https://doi.org/10.1177/1687814018762462.

[2] Lin, C., Lin, W., Han, Y., et al. (2020). Simulation and experimental study of a new structural rubber seal for the roller-cone bit under high temperature. Advances in Mechanical Engineering, 12(12), 1–13. https://doi.org/ 10. 1177/ 1687814020980645.

[3] Han, Y., Nie, J., Zhu, Z., et al. (2024). Investigation of mechanical properties and oil resistance of hydrogenated-butadiene-acrylonitrile-rubber-based composites across various temperatures. Polymers, 16(23), 3294. https:// doi. org/ 10.3390/polym16233294.

[4] Li, R., Lian, Z., & Wei, W. (2024). Influence of operating temperature on crack growth characteristics and fatigue life prediction of carbon black-filled hydrogenated nitrile butadiene rubber. Polymers, 16(24), 3574. https:// doi. org/ 10. 3390/polym16243574.

[5] Huri, D. (2024). Prediction accuracy of hyperelastic material models for rubber bumper under compressive load. Polymers, 16(17), 2534. https://doi.org/10.3390/polym16172534.

[6] Zhang, J. N., et al. (2018). Strain energy-based rubber fatigue life prediction under the influence of temperature. Royal Society Open Science, 5(10), 180951. https://doi.org/10.1098/rsos.180951.

[7] Zhang, L., Wei, et al. (2021). A novel structure of rubber ring for hydraulic buffer seal based on numerical simulation. Applied Sciences, 11(5), 2036. https://doi.org/10.3390/app11052036.

[8] Liu, D., Yun, et al. (2022). Structural analysis and experimental study on the spherical seal of a subsea connector based on a non-standard O-ring seal. Journal of Marine Science and Engineering, 10(3), 404. https:// doi. org/ 10. 3390/ jmse10030404.

[9] He, S., Peng, Y., Qiu, S., et al. (2024). Sealing performance of sealing structure in a sediment sampler under ultra-high pressure. Scientific Reports, 13(1), 18548. https://doi.org/10.1038/s41598-023-45122-0.

[10] Zeng, M., Zhou, Y., & Ma, Y. (2018). Evaluation of sealing performance of bearing rings of roller-cone bits based on grid-shaped bionic non-smooth surface. Advances in Mechanical Engineering, 10(5), 1–21. https:// doi. org/ 10. 1177/ 1687814018773201.

[11] Zhou, W., Wang, C., Fan, P., et al. (2022). The sealing effect improvement prediction of flat rubber ring in roller bit based on Yeoh_Revised model. Materials, 15(16), 5529. https://doi.org/10.3390/ma15165529.

[12] Ma, Y., Xu, Y., & Chen, Y. (2022). Dynamic characteristics of metal seals in roller cone bits. Lubricants, 10(11), 280. https://doi.org/10.3390/lubricants10110280.

[13] Ma, Y., Li, Z., Yuan, Z., et al. (2024). Multi-field coupling numerical analysis and experimental validation of surface-textured metal seals in roller cone bits. Lubricants, 12(1), 15. https://doi.org/10.3390/lubricants12010015.

[14] Hu, G., et al. (2018). Sealing failure analysis on V-shaped sealing rings of an inserted sealing tool used for multistage fracturing processes. Energies, 11(6), 1432. https://doi.org/10.3390/en11061432.

[15] Wu, J. B., Li, et al. (2024). Study on the effects of three surface imperfections on the performance of O-ring seals based on the finite element method. Proceedings of the Institution of Mechanical Engineers, Part C: Journal of Mechanical Engineering Science, 238(20), 10158–10171. https://doi.org/10.1177/0954406224124012.

[16] Chen, Y., Liu, X., & Li, C. (2022). Development of rubber packing element for 105 MPa/215 °C deep-well test packer. Materials, 15(6), 2024. https://doi.org/10.3390/ma15062024.

[17] Zhou, Z., Zhou, Q., Qin, K., et al. (2023). The particle breakage effect on abrasive wear process of rubber/steel seal pairs under high/low pressure. Polymers, 15(8), 1857. https://doi.org/10.3390/polym15081857.

[18] Zhou, Q., Li, et al. (2021). Transitions of wear characteristics for rubber/steel seal pairs during the abrasive wear process. Tribology Letters, 69(3), 1–13. https://doi.org/10.1007/s11249-021-01465-7.

[19] Qin, K., et al. (2019). Non-uniform abrasive particle size effects on friction characteristics of FKM O-ring seals under three-body abrasion. Tribology International, 136, 216–223. https://doi.org/10.1016/j.triboint.2019.03.033.

[20] Kuang, Y., Fan, P., Dong, Z., et al. (2023). Research on Yeoh-Revised hyperelastic constitutive model considering the volume almost incompressible premise for rubber materials. Journal of Elastomers & Plastics, 55(7), 1123–1151. https:// doi.org/10.1177/00952443221147408.

[21] Destrade, M., Dorfmann, L., & Saccomandi, G. (2022). The Ogden model of rubber mechanics: 50 years of impact on nonlinear elasticity. Philosophical Transactions of the Royal Society A: Mathematical, Physical and Engineering Sciences, 380(2234), 20210332. https://doi.org/10.1098/rsta.2021.0332.

[22] Jing, Y., Yuan, Z., He, K., et al. (2026). Sealing performance of O-ring under coupled thermo-mechanical conditions. Mechanical Sciences, 17(1), 123–139. https://doi.org/10.5194/ms-17-123-2026.